Characterisation of strain localisation under cyclic loading at 450 °C by SEM-DIC in a PM Ni-based superalloy

Y. Zhao[1, 2], R. Jiang[1, 2, 3], A. Harte[4], D.J. Bull[3], P.A.S. Reed[3]*

[1] Key Laboratory of Aero-engine Thermal Environment and Structure, Ministry of Industry and Information Technology, College of Energy and Power Engineering, Nanjing University of Aeronautics and Astronautics, Nanjing, 210016, PR China

[2] Jiangsu Province Key Laboratory of Aerospace Power System, College of Energy and Power Engineering, Nanjing University of Aeronautics and Astronautics, Nanjing, 210016, PR China

[3] Materials Research Group, Faculty of Engineering and the Environment, University of Southampton, Highfield, Southampton, SO17 1BJ, UK

[4] School of Materials, University of Manchester, Oxford Road, Manchester, M13 9PL, UK

*Corresponding author. Email: rjiang@nuaa.edu.cn

Abstract:

In this study, the strain localisation under cyclic loading in an advanced powder metallurgy Ni-based superalloy at 450°C was characterised by SEM-DIC, and the related deformation substructures were characterised by electron channelling contrast imaging under controlled diffraction conditions (cECCI). The results indicate strain mainly accumulates in slip/strain bands due to dislocation slip on the {111} plane, and the strain saturates at 1,000 cycles with no evident increase in strain value within strain bands or strain band density from 1,000 cycles to 10,000 cycles. Analysis of the strain components in the local coordinates associated with each strain band shows the strain band mainly consists of shear strain ε_{xy} along the strain band and transverse strain ε_{yy} normal to the strain band. The strain bands can transmit through, be deflected, or be blocked at grain boundaries depending on the grain boundary characteristics and the

neighbouring grain orientation. Comparing the strain bands obtained by SEM-DIC and deformation substructures obtained by cECCI shows that the strain bands originate from underlying continuous slip bands which show the sheared γ' within the slip bands and dislocation pairs looping around the γ' precipitates, but the deformation localised in the discontinuous slip bands is not well characterised by SEM-DIC at this lateral resolution of strain.

Keywords: Ni-based superalloys; Fatigue; Strain localisation; Digital image correlation; Slip system

1 Introduction

Powder metallurgy (PM) Ni-based superalloys have been widely used for high pressure turbine disc rotor applications in aeroengines due to their excellent combined properties, i.e. high strength at elevated temperatures, good resistance to fatigue, creep, oxidation and corrosion [1-5]. Among all the properties of PM Ni-base superalloys for disc applications, fatigue is one of the most important, often limiting the overall service life, due to the centrifugal force and vibration during engine operation, particularly at the disc root fixing which is used to secure the turbine blade [4, 6, 7]. Understanding the fatigue failure mechanisms is important to improve lifing methodology for disc components and develop more advanced alloys for disc application.

The fatigue failure process is closely related to the strain localisation under the cyclic load arising from the manufacturing defects and/or microstructural inhomogeneity in disc alloys [8-12]. To understand the fatigue failure mechanisms and to develop and validate crystal plasticity finite element models, there is a requirement to quantitatively assess the localised strain at the grain level and its dependency on grain orientation and the neighbouring grains/microstructures under the relevant in-service temperatures and loading conditions [13, 14]. Although great efforts have been made to characterise the localised strain, it is still quite challenging to obtain the localised strain at elevated temperatures at the grain level with sub-micron resolution.

Digital image correlation (DIC) is a robust tool to measure full-field in-plane strain

by correlating the random speckle pattern in images taken before and after deformation [15]. The obtained spatial resolution of strain distribution is closely related to the employed speckle patterns, the obtained pixel size (length/pixel) which is dependent on the image-capturing facilities, and parameters such as subset size and step size used for the correlation process [15-18]. Recently, SEM has been employed to capture images for DIC analysis with a much higher pixel resolution compared with images taken by optical cameras, although errors and noise may arise from the image drifting and electron beam distortion during the imaging process [19-22]. Although higher image pixel resolution can be achieved by SEM, the obtained strain spatial resolution is limited by the speckles used for DIC. In a recent publication, Fabio Di Gioacchino et al. [22, 23] applied nanometer size gold particles on a stainless steel surface via a re-modelling process, and achieved a strain spatial resolution at the sub-micron scale. Stinville et al. [21, 24] also achieved a similar strain resolution at sub-micron scale in a Ni-based superalloy using secondary γ' as a natural speckle under tension and compression loading, and found that strain was significantly localised at the slip band adjacent and parallel to twin boundaries (TBs). But these studies were all conducted at room temperature. For strain characterisation at elevated temperatures using DIC, the thermal stability of the speckles (no degradation can occur during the tensile/fatigue tests) is critical to obtain reliable strain distributions. J.L. Walley [25] used electron beam lithography to produce a suitable surface speckle pattern of hafnium oxide with a size of 0.45-0.7μm for strain measurement in Ni-based superalloy Rene104 using DIC at elevated temperatures but the employed hafnium oxides are not small enough and too sparse to get the strain distribution in slip bands. Garrett J. Pataky [26] utilized air blasting alumina particles with a size of 0.3μm and investigated the strain localisation in a Ni-based superalloy Haynes 230 in vacuum, the intergranular strain was clearly captured, but the intragranular strain distribution was not well characterised (which is probably due to the speckle quality issue). More recently, Stinville [27] used the oxide scale that developed in the polycrystalline Ni-based superalloy Rene 88DT at service temperature as a speckle pattern for μm scale resolution strain measurements. Mello [28] applied Ti nano-powder on the surface of the Ni-based superalloy RR1000 as a

speckle pattern to obtain strain distribution. Both studies captured the strain localisation clearly in the slip bands at elevated temperatures, although the analysis of strain localisation only focused on the strain component ε_{xx}, which is along the slip band.

In this study, the strain localisation under cyclic loading in a Ni-based superalloy alloy, i.e. low solvus, high refractory (LSHR) alloy, at the disc bore temperature has been characterised by SEM-DIC analysis. The related deformation microstructures are carefully characterised using electron channelling contrast imaging under diffraction conditions (cECCI), and the nature of the strain components (ε_{xx}, ε_{xy}, ε_{yy}) and the slip transmission behaviour is discussed.

2 Materials and experimental procedures

The LSHR alloy used in this study was provided by NASA. Composition (in wt.%) of the LSHR alloy is 12.5Cr, 20.7Co, 2.7Mo, 3.5Ti, 3.5Al, 0.03C, 0.03B, 4.3W, 0.05Zr, 1.6Ta, 1.5Nb, Ni bal. Specimens used for fatigue tests were extracted from a turbine disc which was fabricated by canning atomized LSHR alloy powder followed by hot isostatically pressing, extruding and isothermally forging. The extracted specimens were supersolvus heat treated and followed by a two−stage aging heat treatment to modify the precipitation of secondary γ'. Details of the heat treatment process can be found in [3]. The obtained LSHR alloy has an average grain size of 38.4±18.1 μm and average secondary γ' size of 153±29 nm based on a measurement of 569 grains and 304 precipitates respectively using planimeter procedure according to a previous study [3].

Fatigue tests were conducted on plain bend bar (4 mm × 4 mm × 55 mm) specimen under three-point bend loading on an Instron 8501 hydraulic testing machine at 450°C in air with a 5 Hz sine waveform and a load ratio of 0.1. The span between the top two rollers is 40 mm with the bottom roller at the mid span position. A schematic diagram of the fatigue test set-up is shown in Fig. 1(a). The applied load was chosen to produce a maximum strain of ~0.8% on the top central surface based on a finite element elastic-plastic simulation. Before the fatigue test, the specimen top surface was ground and polished and then etched by Kalling's reagent (80 ml HCl + 40 ml CH_3OH + 40 g $CuCl_2$)

for 1s to remove the surface residual deformation layer for electron backscatter diffraction (EBSD) mapping at the top central surface. A step size of 1.2μm and a grain boundary (GB) tolerance angle of 2° were employed for orientation mapping with EBSD using the HKL Channel 5 software package in JEOL FEG 6500F SEM. Fig. 1 (b) presents the maximum Schmid factor (SF) map for the EBSD mapped region considering the tensile load direction is parallel to the longitudinal direction of the specimen. Two areas of interest (AOI) were chosen for the following strain characterisation using SEM-DIC. The criterion for choosing these AOIs is that the AOI should contain a large grain with high SF and have a long TB as grains with these characteristics are more likely to initiate a fatigue crack based on the studies presented in the literature [8]. Micro-hardness indentation was introduced at the edge of the top central surface to act as a fiducial to locate the AOI. After orientation mapping with EBSD, the specimen was deeply etched by Kalling's reagent for 60 s to reveal secondary γ'. Then the specimens were put into a furnace at 450 °C in air for 8 hours to pre-oxidise the γ matrix, which stabilised the speckle patterns (i.e. the holes left when secondary γ' were etched off) at the investigated temperature during the fatigue test and provided a stable speckle pattern for the following DIC analysis. Fig. 1 (c) shows the secondary γ' after the pre-oxidation exposure. Before the fatigue tests, SEM image arrays were taken from both AOIs to use as reference images for DIC analysis in JEOL FEG 6500F SEM. The conditions used for SEM imaging are shown in Table 1 according to the guideline proposed by [19, 22, 29]. When reference images have been captured, the fatigue tests were performed at 450 °C for 1,000 cycles → 3,000 cycles → 5,000 cycles → 10,000 cycles, to observe strain localisation in the early stage of fatigue life (crack initiation stage). After each interruption of the fatigue test, the deformation images were taken from the AOIs using the same imaging conditions as shown in Table 1. At the end of the fatigue test, the specimen was mechanically polished using OPS for 3 minutes to remove the etched layer followed by polishing with running water for another 20 minutes to obtain scratch-free and clean surface for cECCI to observe the deformation substructures. The cECCI was conducted using a Zeiss Sigma FEG-SEM with a Gemini column at an accelerating voltage of 30 kV in high current

mode. A Kleindiek E5AT eucentric substage with precise specimen tilt and rotation axes was used to position the specimen in accurate well-defined channelling conditions. The tilt and rotation angles for well-defined channelling conditions were determined by measuring the crystal orientations with EBSD and then applying the software TOCA to simulate the electron channelling patterns for different stage positions. More details about the theory and application of cECCI in characterisation of deformation substructures such as dislocations and stacking fault can be found in a review by S. Zaefferer [30] and a recent article by A. Harte [31].

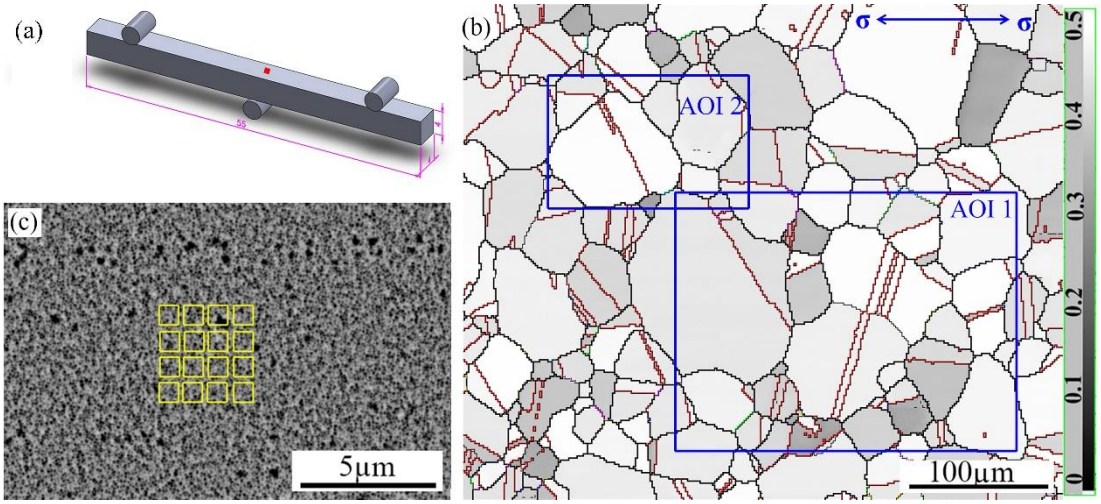

Fig. 1 (a) Schematic diagram of the set-up of the three-point bending fatigue test; (b) Schmid factor map for the top central surface (as indicated by the red square shown in (a)), which contains two AOI for SEM-DIC study of strain localisation; (c) morphology of speckle pattern after pre-oxidation exposure. The yellow squares show the size of the subsets (i.e. 21pixels × 21 pixels or 0.656 μm × 0.656 μm) used for DIC analysis.

Table 1 Imaging parameters in JOEL SEM JSM6500F

Imaging mode	Acceleration voltage	Probe current spot size	Imaging time	Working distance	Image size
BEI	15kV	13	80 s	8.7mm	1280×1024

The obtained SEM images from each AOI were stitched in an open source software Fiji (Image-J). The commercial DIC software MatchID was used for the displacement and strain analysis. The parameters used for strain analysis by DIC are presented in Table 2. More details about these parameters and the noise assessment of

this SEM-DIC technique can be found in [17].

Table 2 Parameters used for strain analysis by DIC

Subset	Step size	Correlation algorithm	Interpolation	Shape functions	Pre-smoothing	Strain window
33×33 pixels	7 pixels	ZNSSD	Bicubic spline	Quadratic	Gaussian 5	3

3 Results and discussion

Fig. 2 (a) presents the strain ε_{xx} in AOI region 1 after 1,000 loading cycles in terms of the global coordinates (i.e. the x axis is parallel to the applied tensile load direction). It should be mentioned that a bandpass filter was applied in the FFT domain to remove the vertical and horizontal noise strips in the strain maps as shown in our previous study [32]. As AOI region 2 shows similar results as AOI region 1, the following analysis concentrates on AOI 1. The obtained grain boundaries from orientation mapping with EBSD are overlaid on the ε_{xx} strain map. The calculated {111} plane slip traces based on EBSD measurement and the corresponding activated slip systems determined by comparing the calculated {111} slip traces and the strain bands in combination with the SF analysis are labelled on the ε_{xx} strain map, and the grains are numbered as shown in Fig. 2 (c). For the reason that three slip systems on the same {111} slip plane share the slip trace, the slip system possess highest Schmid factor is assumed as the activated slip system.A summary of the calculated SF of the activated slip system, maximum SF (SF_{max}) and the corresponding slip system, the calculated {111} slip traces (defined by the inclination angle (β_c) between calculated {111} slip trace at specimen surface and tensile load direction), and the measured slip traces (defined by the inclination angle (β_m) between the strain bands obtained by DIC and the tensile load direction) is presented in Table 3.

Table 3 Summary of the calculated SF, SFmax, calculated {111} slip traces and measured slip traces

Grain ID	Activated slip system	SF	SF_{max}	β_c	β_m	$\lvert\beta_c-\beta_m\rvert$	Slip system with SF_{max}
G1*	(1-11)[110]	0.44	0.453	120.7	120.9	0.2	(11-1)[-110]
	(-111)[01-1]	0.438	0.453	42.4	41.3	1.1	
G2	(-111)[01-1]	0.44	0.44	121.1	120.4	0.7	
G3	(-111)[101]	0.462	0.462	115.5	115.4	0.1	
G4*	(-111)[110]	0.372	0.402	25.8	25.4	0.4	(111)[10-1]
	(111)[10-1]	0.402	0.402	51	51.1	0.1	
G5*	(11-1)[011]	0.437	0.495	71.9	73.3	1.4	(111)[01-1]
G6*	(11-1)[011]	0.36	0.469	74.8	73.3	1.5	(111)[01-1]
G7	(111)[01-1]	0.474	0.474	71.4	66.3	5.1	
G8	(11-1)[1-10]	0.483	0.483	38.9	38.5	0.4	
G9	(111)[10-1]	0.498	0.498	110.2	109.9	0.3	
G10	(111)[10-1]	0.498	0.498	109.7	109.9	0.2	
G11*	(11-1)[1-10]	0.387	0.463	25.8	25.2	0.6	(-111)[01-1]
G12	(1-11)[110]	0.43	0.43	146.1	146.3	0.2	
G13*	(111)[10-1]	0.369	0.385	121.1	119.3	1.8	(-111)[110]
G14*	(-111)[101]	0.41	0.41	103.2	102.8	0.4	(-111)[101]
	(1-11)[011]	0.36	0.41	51.3	51.5	0.2	
G15	(11-1)[011]	0.437	0.437	72.3	71.6	0.6	(11-1)[011]
G16*	(11-1)[011]	0.368	0.472	74.9	72.5	2.4	(111)[01-1]

Note: * next to grain ID indicates that activated slip system is not the slip system with the highest SF in this grain or the active slip systems include the slip system whose SF is not the highest.

As shown in Fig. 2 (a), the SEM-DIC is capable of characterising strain localisation under cyclic loading at the grain level with a sub-micron resolution. Strain localisation is expressed as bands with concentrated strain (analogue to slip bands,

hereafter named as strain bands). Strain bands are predominantly parallel to calculated {111} slip traces and TB with a deviation angle <5° (in most cases, <2°). The strain distribution at 450 ℃ is similar to that at room temperature as shown in [17]. Multiple sets of strain bands with different orientation (corresponding to different {111} slip plane traces) can be found in some relatively large and/or softly orientated grains such as grain 1. When checking the strain band transmission in the AOI grain by grain, it is interesting to notice that the strain bands transmit through the low angle grain boundaries (LAGB) (which have a misorientation of <15 ° as confirmed by EBSD analysis) with little deflection as indicated by the yellow arrows, whereas strain bands apparently deflect at high angle grain boundaries (HAGB) and TBs as indicated by the red arrows. The interaction between slip bands and GBs with different characters is similar to an FCC model alloy such as pure Cu [33]. It should be noted that the transitional region of the strain bands in grain 6 is parallel to none of the calculated {111} slip traces, indicating a cubic slip system may be activated to accommodate the deformation incompatibility, which was also observed in similar disc alloys such as RR1000 [28]. From the ε_{xx} strain map in Fig. 2 (a), some of the strain bands diminish when approaching GBs or within a grain, indicating the deformation may only be confined within certain regions within the grain rather than spread through the whole grain [34].

Fig. 2 (b) – (d) shows ε_{xx}, ε_{yy}, and ε_{xy} distribution in AOI 1 after 10,000 cycles. There was no evident increase in strain value within strain bands or strain band density from 1,000 cycles to 10,000 cycles, which was determined by performing the DIC analysis using images at 1,000 cycles as reference images. In ε_{yy} and ε_{xy} strain maps, strain bands can also be discerned in the same region as shown in ε_{xx} strain map, indicating the strain has multiple components. Morphology of the slip bands are shown in Fig. 2 (f) – (i). It is seen that the slip band cuts through secondary γ'. However, the interaction between slip band and secondary γ' is not as clear as observed at room temperature [17].

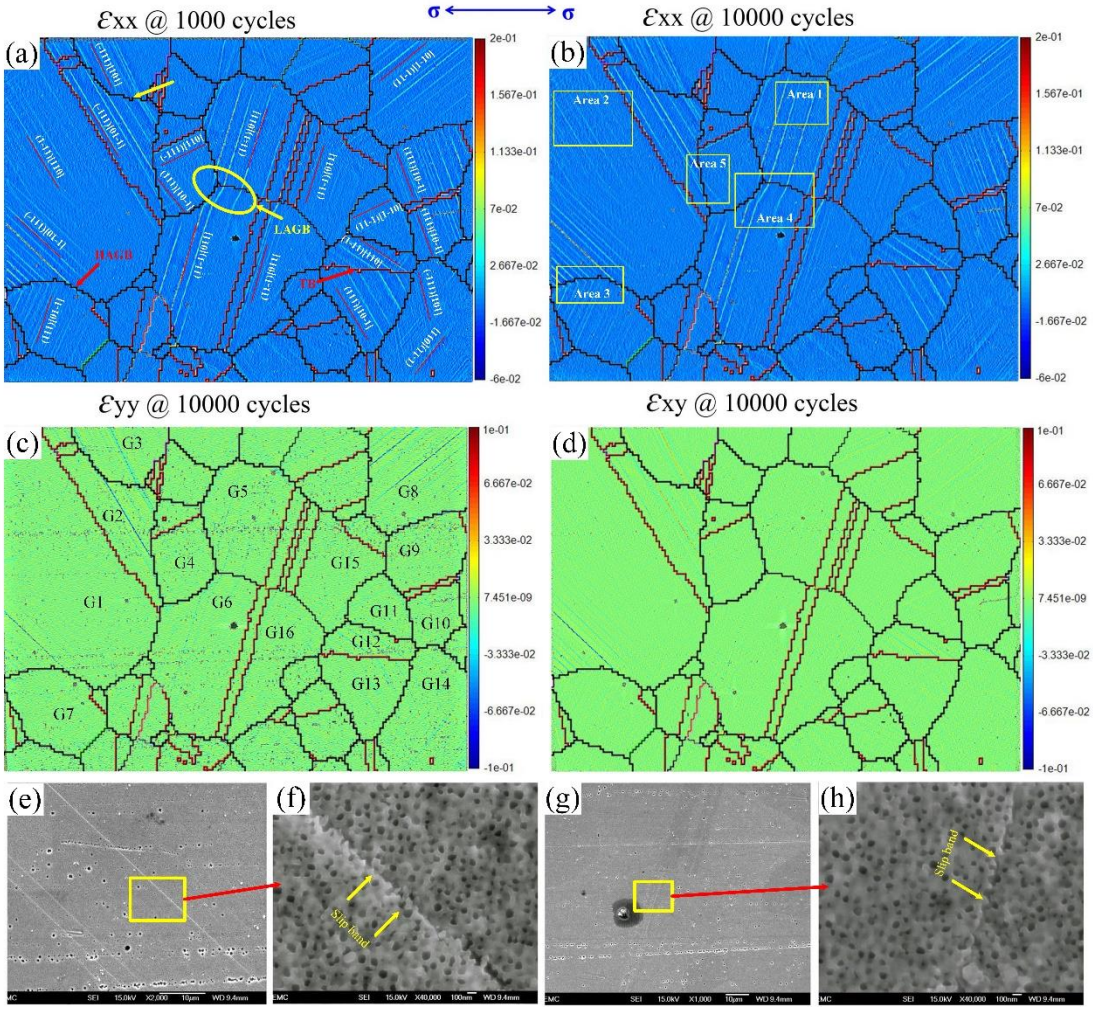

Fig. 2 (a) ε_{xx} strain map at 1,000 cycles; (b) ε_{xx}, (c) ε_{yy} and (d) ε_{xy} strain map at 10,000 cycles; (e)-(f) slip band morphology at 10,000 cycles.

As plastic deformation arises from dislocation motion once the critical resolved shear stress on a specific slip system has been achieved, it is valuable to find out the shear strain associated with the slip system from the in-plane strain measurement by SEM-DIC. A Matlab script has been written to convert the strain field in the global coordinates associated with the tensile load direction to the local coordinates associated with each strain bands (i.e. x axis is parallel to the strain band and y axis is perpendicular to the strain band) in each grain. The Matlab script can detect the strain bands in the global coordinates and then find out the inclination angle between the strain bands and tensile load direction. Once the angle between a strain band and the tensile load direction is known, then the strain distribution can be expressed in the local coordinates.

The Matlab script used for this strain conversion is included as Appendix. The detected angles for each parallel set of the strain bands are shown in Fig. 3 (a). It should be noted that some weak strain bands which can be seen in Fig. 2 (a) and (b) disappear or are not as clear as shown in Fig. 3 (a), this is probably caused by the noise filter applied when conducting the band detection to measure the angle between strain bands and tensile load direction. Fig. 3 (b)-(d) show the converted strain distribution in the local coordinates after 10,000 loading cycles. It is worth emphasising that each parallel set of strain bands have their own local coordinates. As shown in Fig. 3 (b)-(d), the slip band mainly consists of shear strain ε_{xy} along the slip band and transverse strain ε_{yy} normal to the slip band. The shear strain can be rationalised to dislocation motions, whereas the transverse strain may arise from the in-plane stretch due to the dislocation out-of-plane motion which causes slip extrusion at the surface [17]. In addition, as the test was conducted at 450 °C, absorption of oxygen at the extrusion of the slip band at the surface results in slip irreversibility, leading to evident transverse strain[35]. In terms of ε_{xx} distribution, it is not evident in most grains. The existence of ε_{xx} strain may be related to the slip band impingement at the grain boundary which may result in subsequent back stresses acting on dislocation sources and the activated deformation in neighbouring grains, which introduces tension or compression to the slip band [36].

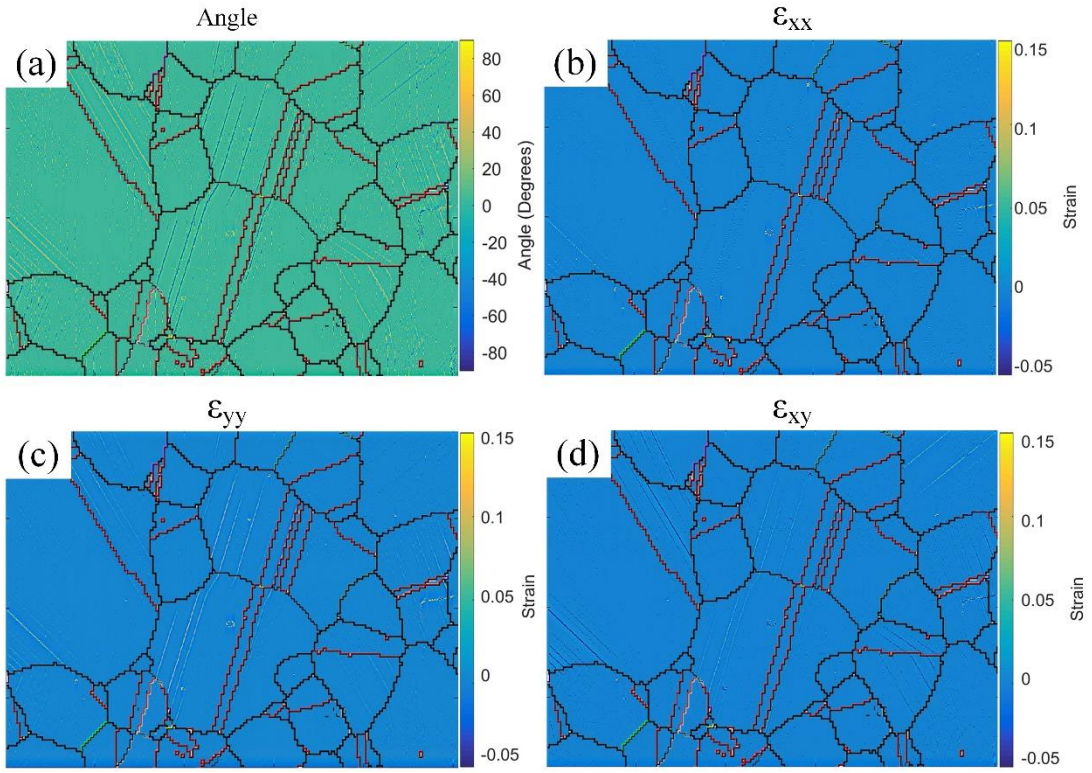

Fig. 3 (a) Angles between the strain bands and tensile load direction; (b) ε_{xx}, (c) ε_{yy} and (d) ε_{xy}, distribution in local coordinates after 10,000 loading cycle.

Fig. 4 presents the deformation substructures in the 5 regions labelled in Fig. 2 (b) obtained by cECCI. Fig. 4 (a)-(c) shows the deformation substructures in region 1, from which we can see the slip band forms adjacent and parallel to TB. This is consistent with Stinville's observation in Rene88DT and our previous study on the LSHR alloy tested at room temperatures [37]. The continuous slip bands correspond to the strain bands shown in Fig. 2. Between the continuous slip bands, quite a few discontinuous slip bands (DSB) are located between the continuous slip bands, but these DSBs cannot be revealed from the strain maps, indicating relatively less strain. More intensive deformation can be seen in the continuous slip bands along with the sheared γ' within in the slip bands and dislocation pairs looping around the γ'. Apart from the slip bands and dislocations, another substructure is the stacking fault which is found in region 2 shown in Fig. 2 (d) and is presented in Fig. 4 (d) and (e). The stacking fault as a plane defect in Ni-based superalloys, which may be inherent from heat treatment process or form under the fatigue loading, appears to be parallel to the {111} slip plane and can

shear cut through the γ'. As shown in Fig. 4 (e), the stacking fault can intersect with other stacking faults with different orientation, slip bands and dislocation, giving rise to locally higher deformation indicated by the higher brightness. Fig. 4 (f) presents the deformation substructures in region 3 where slip deflects at a HAGB. It can be seen that the deformation in the continuous slip bands in this region is quite diffuse, especially in the neighbouring grains adjacent to the grain boundary where the deflection occurs. In addition, plenty of dislocation pairs looping around the γ' can be observed between the diffused but continuous slip bands. Fig. 4 (g) and (h) shows the slip transmission through a LAGB. It is interesting to notice that a segment of the slip bands adjacent to the LAGB deviates from the {111} slip band immediately after transmission through the LAGB. However, the deformation substructures within this transitional slip band segment are seemingly the same as observed in the {111} slip bands. Fig. 4 (i) shows a slip band impingement at a grain boundary, and results in enhanced strain localisation along the grain boundary and in the adjacent neighbouring grain as highlighted by the ellipse, which is consistent with the higher localised strain along the grain boundary shown in region 5 in Fig. 2 (b).

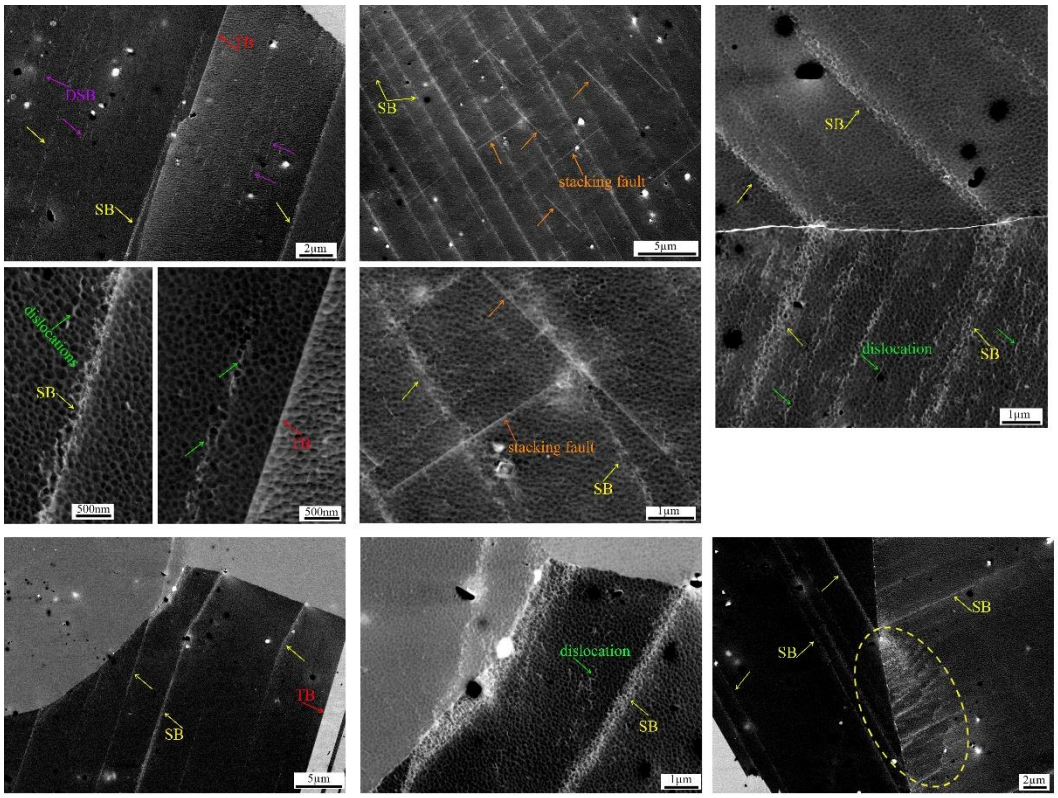

Fig. 4 Deformation substructures in (a)-(c) region 1, (d) and (e) region 2, (f) region 3, (g) and (h) region 4, and (i) region 5 shown in Fig. 2 (b)

As shown in Figs. 2-4, strain mainly accumulates in slip bands due to dislocation slip on the {111} plane, and the slip bands can transmit through or be deflected or be blocked at grain boundaries depending on the GB character and the neighbouring grain orientation. The strain accumulation in the slip bands and the development of slip bands are usually associated with fatigue crack initiation and early propagation [37]. It is widely observed in polycrystalline Ni-based superalloys that cracks predominantly initiate from the slip bands adjacent and parallel to TB in large grains and the slip bands are usually associated with slip system with highest SF[17]. However, the short crack may not always propagate along the slip bands with highest SF due to the constraint of neighbouring grains and the local deformation incompatibility (or the requirement of the geometrical compatibility)[37]. Similarly, as shown in Fig. 2 and the calculated SF of the activated slip systems associated with strain bands in Table 3, especially for these interconnected strain bands, not all the slip systems associated with strain bands have highest SF.

For those interconnected strain bands which are supposed to associate with early crack propagation, the geometric compatibility factor m' (which is used to describe the transmission of the slip bands in adjacent grains) was calculated based on Equation (1) as suggested in Luster and Morris' study to analyse the slip transmission [38]:

$$m' = \left|\left(n_{sp1} \cdot n_{sp2}\right) \bullet \left(d_{spd1} \cdot d_{spd2}\right)\right| \tag{1}$$

Among them, n_{sp1}, n_{sp2} are the unit normal vectors of the slip plane; d_{spd1}, d_{spd2} are the unit vectors of the slip direction. The value of the geometric compatibility factor m' ranges from 0 to 1; the higher the m', the easier for the slip transmission to occur. Meanwhile, the tilt angle α and twist angle β of two slip planes (which are located in two neighbouring grains respectively) were also calculated to analyse the slip transmission based on Zhai [39] and Baptiste's [40] definition as schematically shown in Fig. 5 and Equations (2) and (3):

$$\alpha = \arccos\left[\left(l_{gb} \times n_{sp1}\right) \bullet \left(l_{gb} \times n_{sp2}\right)\right] \tag{2}$$

$$\beta = \arccos\left[\left(n_{Surface} \times n_{sp1}\right) \bullet \left(n_{Surface} \times n_{sp2}\right)\right] \tag{3}$$

Among them, l_{gb} and $n_{Surface}$ are the unit normal vector of the grain boundary and the unit normal vector of the surface respectively.

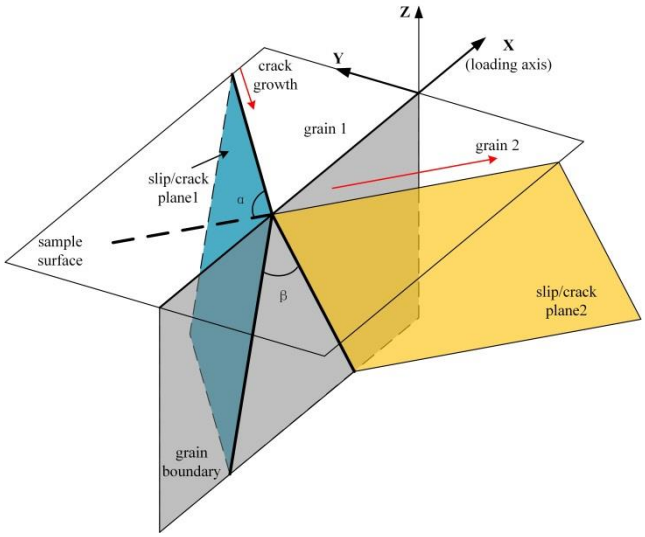

Fig. 5 Schematic diagram of the interaction between the slip plane in neighbouring grans [39].

According to the measurement results of SEM-DIC and EBSD, the geometric compatibility factor m', the tilt angle α and the twist angle β of the interconnected strain bands located in neighbouring grain pairs are analysed and the results are presented in Fig. 6. As shown in Fig. 6 (a), the geometric compatibility factor and the tilt angle roughly shows an inversely proportional relationship, which demonstrates that low tilt angle is linked to relatively easy slip transmission. Fig. 6(b) shows the relationship between geometric compatibility factor and the twist angle. For grain pairs G1-G7, G5-G6, G12-G13 and G15-G16, the geometric compatibility factor and the twist angle basically also show an inversely proportional relationship, indicating the low twist angle may be related to easy slip transmission as well. However, the twist angles of grain pairs G2-G4 and G13-G14 are relatively low, indicating the easy slip transmission, whereas the geometric compatibility factor and the tilt angle for G2-G4 and G13-G14 indicate difficult slip transmission in these two grain pairs. This discrepancy may arise

from the assumption that grain boundary was perpendicular to the specimen surface when calculating the twist angle. Meanwhile, this may also indicate the activation and slip transmission of slip system will be influenced by some other influential factors such as the constraint of surrounding grains and subsurface grains rather than just two neighbouring grains.

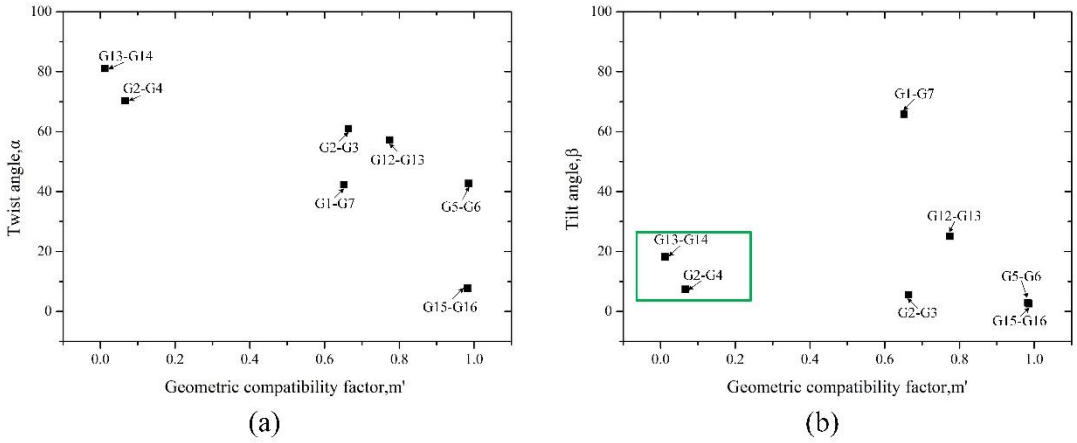

Fig. 6 The relationship between the geometric compatibility factor m′ and (a) tilt angle α, and (b) twist angle β of slip planes in neighbouring grains.

Conclusions

In this study, the strain localisation under cyclic loading at 450°C was characterised by SEM-DIC in an advanced disc alloy LSHR, using the pre-oxidised speckle patterns, and the related deformation substructures were characterised by cECCI.

The following conclusions can be drawn based on aforementioned results and discussion:

(1) SEM-DIC using pre-oxidised speckle patterns is capable of characterising strain localisation under cyclic loading at the grain level with a sub-micron resolution. Strain mainly accumulates in slip bands due to dislocation slip on the{111} planes, and the strain bands can transmit through, be deflected or be blocked at grain boundaries depending on the GB character and the neighbouring grain orientation. Strain seems to

saturate at 1,000 cycles. There was no evident increase in strain value within strain bands or strain band density on cycling from 1,000 cycles to 10,000 cycles.

(2) The strain band mainly consists of shear strains ε_{xy} along the strain band and transverse strains ε_{yy} normal to the strain band in the local coordinates. The shear strain can be rationalised in terms of dislocation motions, whereas the transverse strain may arise from the in-plane stretch due to the dislocation out-of-plane motion which causes slip extrusion at surface.

(3) Strain bands obtained by SEM-DIC arise from underlying continuous slip bands that show the sheared γ' within in the slip bands and dislocation pairs looping around the γ' precipitates, but the deformation localised in the discontinuous slip bands cannot be well characterised by SEM-DIC at this lateral resolution of strain.

Dataset Statement

The data that support the findings of this study are available from the corresponding author upon reasonable request.

Declaration of competing interest

The authors declare that they have no known competing financial interests or personal relationships that could have appeared to influence the work reported in this paper.

Acknowledgement

RJ would like to thank the National Natural Science Foundation of China (No. 51805251; 11872204), the Natural Science Foundation of Jiangsu Province (No. BK20180434) for financial support. PAS would like to thank the Engineering and Physical Sciences Research Council (No. EP/M000710/1) in the UK for financial support. Thanks are also due to Dr. Tim Gabb at NASA Glenn Research Centre for the supply of LSHR alloy, to Prof F. Pierron for provision of the MatchID software, and to Prof M. Preuss for his assistance of cECCI characterisation of deformation substructures in LSHR alloy.

References:

[1] Reed RC. The Superalloys: Cambridge University Press; 2006.

[2] Pollock TM, Tin S. Nickel-Based Superalloys for Advanced Turbine Engines: Chemistry, Microstructure and Properties. Journal of Propulsion and Power 2006;22:361-74.

[3] Jiang R, Everitt S, Lewandowski M, Gao N, Reed PAS. Grain size effects in a Ni-based turbine disc alloy in the time and cycle dependent crack growth regimes. International Journal of Fatigue 2014;62:217-27.

[4] Jiang R, Song YD, Reed PA. Fatigue crack growth mechanisms in powder metallurgy Ni-based superalloys—A review. International Journal of Fatigue 2020;141:105887.

[5] Jiang R, Zhang LC, Zhang WT, Zhang Y, Chen Y, Liu JT, et al. Low cycle fatigue and stress relaxation behaviours of powder metallurgy Ni-based superalloy FGH4098. Materials Science and Engineering: A 2021;817:141421.

[6] Telesman J, Gabb TP, Ghosn LJ, Gayda J. Effect of notches on creep–fatigue behavior of a P/M nickel-based superalloy. International Journal of Fatigue 2016;87:311-25.

[7] Pineau A, Antolovich SD. High temperature fatigue: behaviour of three typical classes of structural materials. Materials at High Temperatures 2015;32:298-317.

[8] Jiang R, Karpasitis N, Gao N, Reed PAS. Effects of microstructures on fatigue crack initiation and short crack propagation at room temperature in an advanced disc superalloy. Materials Science and Engineering: A 2015;641:148-59.

[9] Pang HT, Reed PAS. Microstructure effects on high temperature fatigue crack initiation and short crack growth in turbine disc nickel-base superalloy Udimet 720Li. Materials Science and Engineering: A 2007;448:67-79.

[10] Stinville J-C, Martin E, Karadge M, Ismonov S, Soare M, Hanlon T, et al. Competing Modes for Crack Initiation from Non-metallic Inclusions and Intrinsic Microstructural Features During Fatigue in a Polycrystalline Nickel-Based Superalloy. Metall and Mat Trans A 2018;49:3865-73.

[11] Miao G, Yang X, Shi D. Competing fatigue failure behaviors of Ni-based superalloy FGH96 at elevated temperature. Materials Science and Engineering: A 2016;668:66-72.

[12] Sangid MD. The physics of fatigue crack initiation. International Journal of Fatigue 2013;57:58-72.

[13] Jiang J, Dunne FPE, Britton TB. Toward Predictive Understanding of Fatigue Crack Nucleation in Ni-Based Superalloys. JOM 2017;69:863-71.

[14] Jiang J, Yang J, Zhang T, Zou J, Wang Y, Dunne FPE, et al. Microstructurally sensitive crack nucleation around inclusions in powder metallurgy nickel-based superalloys. Acta Materialia 2016;117:333-44.

[15] Bing P, Kemao Q, Huimin X, Anand A. Two-dimensional digital image correlation for in-plane displacement and strain measurement: a review. Measurement Science and Technology 2009;20:062001.

[16] Dong YL, Pan B. A Review of Speckle Pattern Fabrication and Assessment for Digital Image Correlation. Exp Mech 2017;57:1161-81.

[17] Jiang R, Pierron F, Octaviani S, Reed PAS. Characterisation of strain localisation processes during fatigue crack initiation and early crack propagation by SEM-DIC in an advanced disc alloy. Materials Science and Engineering: A 2017;699:128-44.

[18] Scrivens WA, Luo Y, Sutton MA, Collette SA, Myrick ML, Miney P, et al. Development of Patterns for Digital Image Correlation Measurements at Reduced Length Scales. Exp Mech 2007;47:63-77.

[19] Sutton MA, Li N, Joy DC, Reynolds AP, Li X. Scanning Electron Microscopy for Quantitative Small

and Large Deformation Measurements Part I: SEM Imaging at Magnifications from 200 to 10,000. Exp Mech 2007;47:775-87.
[20] Sutton MA, Li N, Garcia D, Cornille N, Orteu JJ, McNeill SR, et al. Scanning Electron Microscopy for Quantitative Small and Large Deformation Measurements Part II: Experimental Validation for Magnifications from 200 to 10,000. Exp Mech 2007;47:789-804.
[21] Stinville JC, Vanderesse N, Bridier F, Bocher P, Pollock TM. High resolution mapping of strain localization near twin boundaries in a nickel-based superalloy. Acta Materialia 2015;98:29-42.
[22] Di Gioacchino F, Quinta da Fonseca J. Plastic Strain Mapping with Sub-micron Resolution Using Digital Image Correlation. Exp Mech 2013;53:743-54.
[23] Di Gioacchino F, Quinta da Fonseca J. An experimental study of the polycrystalline plasticity of austenitic stainless steel. International Journal of Plasticity 2015;74:92-109.
[24] Stinville JC, Echlin MP, Texier D, Bridier F, Bocher P, Pollock TM. Sub-Grain Scale Digital Image Correlation by Electron Microscopy for Polycrystalline Materials during Elastic and Plastic Deformation. Exp Mech 2015;56:197-216.
[25] Walley JL, Wheeler R, Uchic MD, Mills MJ. In-Situ Mechanical Testing for Characterizing Strain Localization During Deformation at Elevated Temperatures. Exp Mech 2012;52:405-16.
[26] Pataky G, Sehitoglu H. Experimental Methodology for Studying Strain Heterogeneity with Microstructural Data from High Temperature Deformation. Exp Mech 2015;55:53-63.
[27] Stinville JC, Echlin MP, Callahan PG, Miller VM, Texier D, Bridier F, et al. Measurement of Strain Localization Resulting from Monotonic and Cyclic Loading at 650 ∘C in Nickel Base Superalloys. Exp Mech 2017;57:1289-309.
[28] Mello AW, Nicolas A, Sangid MD. Fatigue strain mapping via digital image correlation for Ni-based superalloys: The role of thermal activation on cube slip. Materials Science and Engineering: A 2017;695:332-41.
[29] Kammers AD, Daly S. Digital Image Correlation under Scanning Electron Microscopy: Methodology and Validation. Exp Mech 2013;53:1743-61.
[30] Zaefferer S, Elhami N-N. Theory and application of electron channelling contrast imaging under controlled diffraction conditions. Acta Materialia 2014;75:20-50.
[31] Harte A, Atkinson M, Smith A, Drouven C, Zaefferer S, Quinta da Fonseca J, et al. The effect of solid solution and gamma prime on the deformation modes in Ni-based superalloys. Acta Materialia 2020;194:257-75.
[32] Jiang R, Bull DJ, Evangelou A, Harte A, Pierron F, Sinclair I, et al. Strain accumulation and fatigue crack initiation at pores and carbides in a SX superalloy at room temperature. International Journal of Fatigue 2018;114:22-33.
[33] Li LL, Zhang ZJ, Zhang P, Yang JB, Zhang ZF. Distinct fatigue cracking modes of grain boundaries with coplanar slip systems. Acta Materialia 2016;120:120-9.
[34] Sperry R, Harte A, Quinta da Fonseca J, Homer ER, Wagoner RH, Fullwood DT. Slip band characteristics in the presence of grain boundaries in nickel-based superalloy. Acta Materialia 2020;193:229-38.
[35] R.W. Cahn PH. Physical Metallurgy. Cambridge University Press:1996.
[36] Linne MA, Bieler TR, Daly S. The effect of microstructure on the relationship between grain boundary sliding and slip transmission in high purity aluminum. International Journal of Plasticity 2020;135:102818.
[37] Schaef W, Marx M, Vehoff H, Heckl A, Randelzhofer P. A 3-D view on the mechanisms of short

fatigue cracks interacting with grain boundaries. Acta Materialia 2011;59:1849-61.
[38] Briffod F, Bleuset A, Shiraiwa T, Enoki M. Effect of crystallographic orientation and geometrical compatibility on fatigue crack initiation and propagation in rolled Ti-6Al-4V alloy. Acta Materialia 2019;177:56-67.
[39] Zhai T, Wilkinson AJ, Martin JW. A crystallographic mechanism for fatigue crack propagation through grain boundaries. Acta Materialia 2000;48:4917-27.
[40] Larrouy B, Villechaise P, Cormier J, Berteaux O. Grain boundary–slip bands interactions: Impact on the fatigue crack initiation in a polycrystalline forged Ni-based superalloy. Acta Materialia 2015;99:325-36.